NANO LETTERS
Cite This: Nano Lett. 2018, 18, 6340−6346
Letter
pubs.acs.org/NanoLett

Molecular-Beam Epitaxy of Two-Dimensional In_2Se_3 and Its Giant Electroresistance Switching in Ferroresistive Memory Junction

Sock Mui Poh,[○,†,‡] Sherman Jun Rong Tan,[○,†,‡] Han Wang,[§] Peng Song,[‡,∥] Irfan H. Abidi,[⊥] Xiaoxu Zhao,[†,‡] Jiadong Dan,[†,§] Jingsheng Chen,[§] Zhengtang Luo,[⊥] Stephen J. Pennycook,[†,§,∥] Antonio H. Castro Neto,[∥,#] and Kian Ping Loh*[,‡,∥]

[†]NUS Graduate School for Integrative Sciences and Engineering, Centre for Life Sciences No. 05-01, 28 Medical Drive, 117456 Singapore

[‡]Department of Chemistry, National University of Singapore, Science Drive 3, 117543 Singapore

[§]Department of Materials Science and Engineering, National University of Singapore, 117575 Singapore

[∥]Centre for Advanced 2D Materials and Graphene Research Centre, National University of Singapore, 117546 Singapore

[⊥]Department of Chemical and Biological Engineering, The Hong Kong University of Science and Technology, Clear Water Bay, Kowloon, Hong Kong

[#]Department of Physics, National University of Singapore, 3 Science Drive 2, 117542 Singapore

Supporting Information

ABSTRACT: Ferroelectric thin film has attracted great interest for nonvolatile memory applications and can be used in either ferroelectric Schottky diodes or ferroelectric tunneling junctions due to its promise of fast switching speed, high on-to-off ratio, and nondestructive readout. Two-dimensional α-phase indium selenide (In_2Se_3), which has a modest band gap and robust ferroelectric properties stabilized by dipole locking, is an excellent candidate for multidirectional piezoelectric and switchable photodiode applications. However, the large-scale synthesis of this material is still elusive, and its performance as a ferroresistive memory junction is rarely reported. Here, we report the low-temperature molecular-beam epitaxy (MBE) of large-area monolayer α-In_2Se_3 on graphene and demonstrate the use of α-In_2Se_3 on graphene in ferroelectric Schottky diode junctions by employing high-work-function gold as the top electrode. The polarization-modulated Schottky barrier formed at the interface exhibits a giant electroresistance ratio of 3.9×10^6 with a readout current density of >12 A/cm^2, which is more than 200% higher than the state-of-the-art technology. Our MBE growth method allows a high-quality ultrathin film of In_2Se_3 to be heteroepitaxially grown on graphene, thereby simplifying the fabrication of high-performance 2D ferroelectric junctions for ferroresistive memory applications.

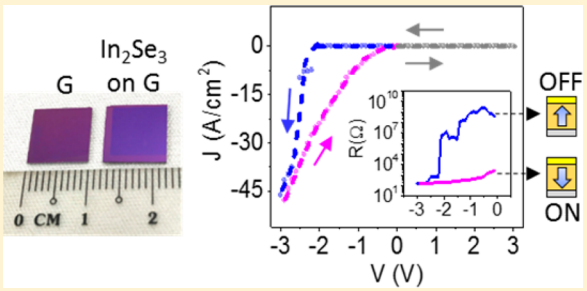

KEYWORDS: *In_2Se_3, two-dimensional materials, molecular-beam epitaxy, ferrorelectric Schottky diode, ferroresistive memory junction, giant electroresistance ratio*

Ferroelectric Schottky diodes (FSDs) with polarization-modulated Schottky barriers are promising for applications in resistive switching memories, but its performance in terms of its on-to-off ratio and readout current densities are much poorer than ferroelectric tunneling junctions (FTJ).[1,2] This is because the insulating properties of oxide-based ferroelectric materials limit the maximum diode current, which precludes the stable detection of memory status using sense amplifiers, especially in miniaturized circuit elements.[1] Using thinner materials to improve current density, however, compromises the ferroelectric properties due to the presence of depolarization field, which strongly suppresses spontaneous polarization in thin materials.[3] The ideal ferroelectric material should, therefore, possess a modest band gap and also the ability to retain spontaneous out-of-plane polarization when scaled down to the ultrathin level. Recently, 2D indium selenide (α-In_2Se_3) was reported to exhibit spontaneous electric polarization.[4−6] Its unique noncentrosymmetric crystal structure leads to an intrinsic stabilization of in-plane and out-of-plane polarizations through dipole-locking,[7] giving rise to multidirectional piezoelectricity for applications such as electronic skin and energy-harvesting cells[4,6] as well as ferroelectricity for switchable diode devices.[5] The ferroelectric properties of In_2Se_3 may provide additional control in applications of optoelectronics,[8−10] photovoltaics,[11−13] and thermoelectrics.[14] To harness its interesting optical and electronic properties, the large-scale

Received: July 2, 2018
Revised: September 6, 2018
Published: September 7, 2018

DOI: 10.1021/acs.nanolett.8b02688
Nano Lett. 2018, 18, 6340−6346

synthesis of ultrathin, high-quality α-In_2Se_3 is needed. To date, only isolated micrometer-sized α-In_2Se_3 crystals had been grown using chemical vapor deposition (CVD)[5,15] and physical vapor deposition (PVD)[4,16,17] approaches. The MBE growth of In_2Se_3 has mostly been reported for thick film[18−21] using indium elemental sources, which is incompatible with the growth of ultrathin films due to its low melting point.

Herein, we report the molecular-beam epitaxy of continuous, centimeter-sized monolayer α-In_2Se_3 on single-layer graphene using the twin evaporation of In_2Se_3 and Se precursors. The optimized growth temperature of 250 °C presents process advantages because it is significantly lower than CVD and PVD growth temperatures, which are typically >600 °C. Our growth method is highly versatile, and the conditions can be tuned to grow monolayer α-In_2Se_3, γ-In_2Se_3, or InSe. Piezoresponse force microscopy (PFM) was used to characterize the ferroelectric properties of as-grown α-In_2Se_3 film of ∼6 nm thickness with coercive voltages observed at +0.5 and −2.5 V. A MBE-grown few-layer α-In_2Se_3-on-graphene structure was readily fabricated into a ferroresistive Schottky diode by using gold as the top electrode, achieving a giant electroresistance with an on-to-off ratio of up to 3.9×10^6, which is comparable with the state-of-the-art FTJs.[22−24] The current density obtained at the reading voltage of −1.4 V is at least 12 A/cm^2, which is sufficient for detection by sense amplifier, even when miniaturized. The on-to-off ratio and readout current density are one of the highest values reported for FSDs,[1,25,26] and unlike FTJs, the fabricated In_2Se_3 ferroelectric junction does not need additional engineering of interface barrier material.[23,24,27]

Monolayer indium selenide was epitaxially grown on single-layer graphene substrate at 250 °C using powdered In_2Se_3 and Se precursors, as shown schematically in Figure 1a. To obtain high-quality α-In_2Se_3 film, a high flux ratio of $Se/In_2Se_3 \approx 6{:}1$ is needed. Keeping all other growth parameters constant, when only In_2Se_3 is evaporated, monolayer InSe is grown instead (Figure S1). This can be attributed to the decomposition of In_2Se_3 in Se-deficient environment.[28] The phases of the grown films were unambiguously determined by Raman spectroscopy.[29,30] For the film grown without Se precursor, four peaks are observed at ∼116, 178, 200, and 227 cm^{-1} (Figure 1b), which can be assigned to the A_1, E, A_1(LO), and A_1 Raman peaks of InSe, respectively.[31] When the film was grown with the coevaporation of In_2Se_3 and Se precursors, pure-phase α-In_2Se_3 could be grown, as judged by the presence of the A_1(LO + TO), A_1(TO), and A_1(LO) Raman signature peaks of α-In_2Se_3[32,33] at ∼108, 176, and 205 cm^{-1}, respectively (Figure 1d). We also investigated the growth condition of $Se/In_2Se_3 \approx 3{:}1$ and obtained the Raman spectrum dominated by peaks associated with InSe but with an extra peak at ∼208 cm^{-1} (black arrow, Figure 1c), which most likely originated from α-In_2Se_3.

The morphology of the films grown under different conditions was analyzed using atomic force microscopy (AFM). In contrast to InSe (Figure 1e), the nucleation density of α-In_2Se_3 is much lower and its grains are much larger, better-faceted, and highly oriented (Figure 1g). However, the AFM of the mixed-phase indium selenide (Figure 1f) shows a similar grain size to that of pure InSe; it is notable that there is buckling of grain boundaries, which may be due to lateral lattice mismatch of InSe and α-In_2Se_3. Such mixed-phase 2D materials can be developed for interesting electronic, chemical, and optical applications.[34−36]

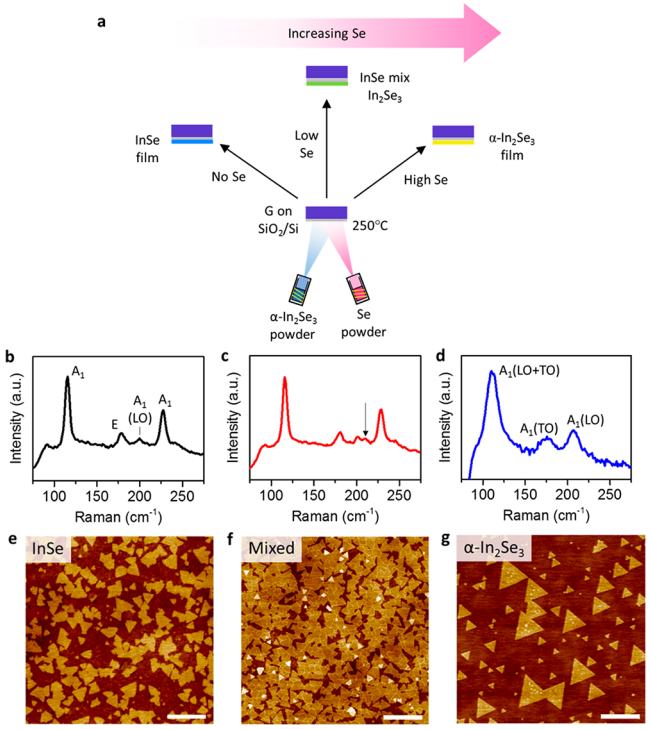

Figure 1. Controlled MBE growth of InSe to In_2Se_3. (a) Schematic illustration of the different growth conditions required to selectively grow the different binary phases of indium selenide. Raman of the (b) InSe grown under condition of only In_2Se_3 precursor, (c) mixed InSe-In_2Se_3 grown with precursor ratio Se/In_2Se_3 = 3:1, and (d) In_2Se_3 grown with precursor ratio Se/In_2Se_3 = 6:1. AFM topography of the as-grown (e) InSe, (f) mixed InSe-In_2Se_3, and (g) In_2Se_3. Scale barss: 400 nm.

The growth mechanism of the α-In_2Se_3 films followed the Frank−van der Merwe growth mode,[37,38] in which lateral growth occurs much faster than vertical growth. We found that the optimum MBE growth of α-In_2Se_3 occurs at 250 °C because further increase in growth temperature results in a high desorption rate of grown In_2Se_3 film (Figure S2). The growth of α-In_2Se_3 at this temperature is sufficient for the grains to coalesce and form continuous monolayer film (Figure 2a−c) with a growth rate of one monolayer in 2 h, which is much faster than the reported >10 h/ML MBE growth rate of monolayer transition metal dichalcogenides (TMDCs).[39,40] We noted that the monolayer α-In_2Se_3 is easily damaged under voltage-biased AFM tip or laser illumination due to its low thermal conductivity[41] and have exploited this property for the precise nanoscale etching and patterning of the ultrathin film[42,43] without the use of any mask or complicated lithography procedure (Figure 2d). The rectangular pattern was etched in the 4 nm thick α-In_2Se_3 with a 10 V biased AFM tip.

Other than studying growth parameters such as substrate temperature and precursor flux ratio, we also investigated the effect of substrate on the phase of the as-grown material, which is especially relevant for In_2Se_3 due to its rich polymorphism. AFM topographic scans show that the grains grown on the epitaxial graphene substrate are well-aligned with 60° orientation. For controlled experiment, we performed the same growth on nonepitaxial SiO_2/Si substrate, a commonly used substrate for CVD growth of single crystal TMDC.[44] A nonlayered growth morphology (Figure 2e) due to the growth of γ-In_2Se_3[33] was obtained, as verified by the Raman signature peaks of this phase

DOI: 10.1021/acs.nanolett.8b02688
Nano Lett. 2018, 18, 6340−6346

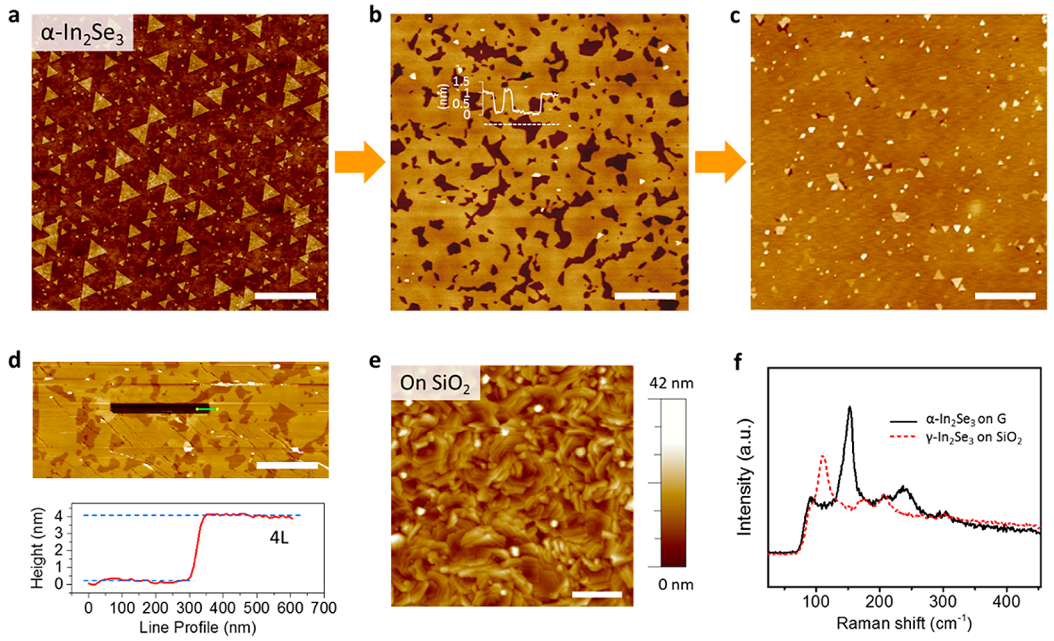

Figure 2. AFM characterization of MBE grown α-In_2Se_3 and γ-In_2Se_3. AFM topography showing the evolution in α-In_2Se_3 morphology as the growth progresses from (a) isolated facets to (b) coalescence and to (c) forming a continuous monolayer. (d) Etched hole of area of 3 μm × 300 nm on the as-grown 4 nm thick α-In_2Se_3 by 10 V-biased AFM contact tip. The bottom plot shows the corresponding height profile. (e) AFM topography of the γ-In_2Se_3 grown on SiO_2/Si substrate and its (f) corresponding Raman spectrum compared to that of α-In_2Se_3 grown on graphene. Scale bars: (a–c) 1 μm, (d) 2 μm, and (e) 400 nm.

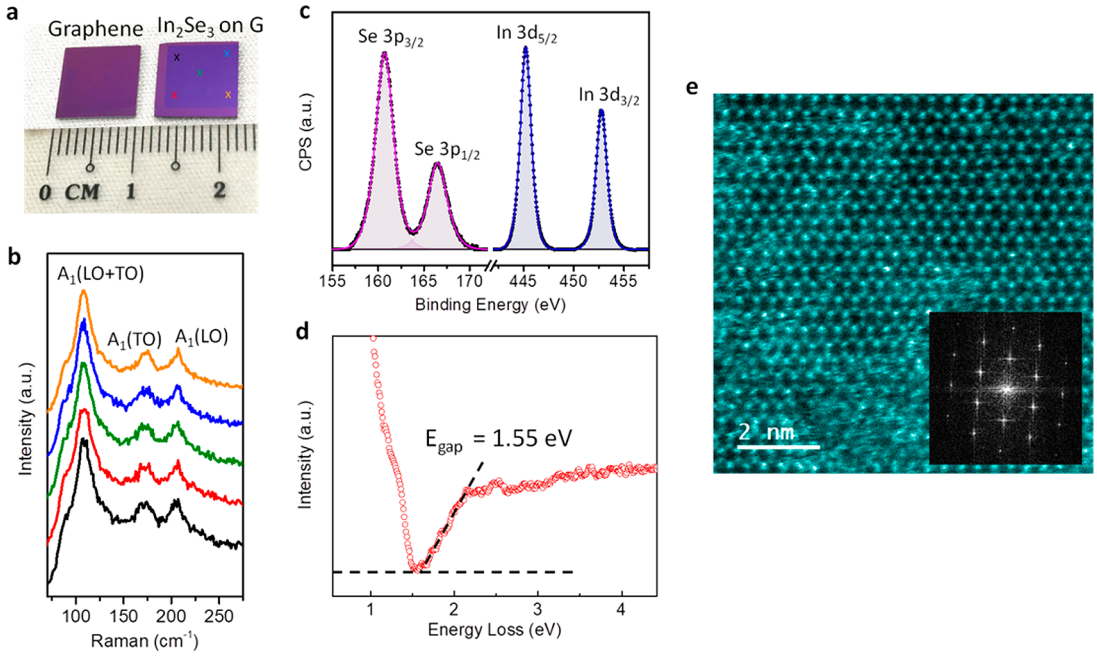

Figure 3. Large-area MBE growth of α-In_2Se_3 and its spectroscopic and microscopic characterizations. (a) Photograph of the 1 cm^2 graphene on SiO_2/Si substrate and ~1 cm^2 MBE grown α-In_2Se_3 on the graphene/SiO_2/Si substrate. (b) Raman spectra of the respective colored spots from the MBE-grown 1 cm^2 In_2Se_3 shown in panel a. (c) XPS of the In 3*d* and Se 3*p* core orbital peaks of the grown α-In_2Se_3 film. (d) HREELS measured at specular angle of the grown α-In_2Se_3 film. The onset indicates the electronic bandgap. (e) STEM-ADF image of the grown α-In_2Se_3 monolayer. The inset shows the corresponding fast Fourier transform image.

at 152, 209, and 237 cm^{-1} (Figure 2f). This shows that for the MBE growth of van der Waals 2D film, a substrate with matching crystal symmetry is required, in agreement with previous MBE studies of 2D transition-metal dichalcogenides.[38,45]

The MBE growth of α-In_2Se_3 film is highly scalable, and we demonstrate it on a 1 cm^2 CVD graphene layer on SiO_2/Si, prepared by the method described in ref 46 (Figure 3a). Raman spectra recorded from random spots on the grown sample are almost identical, attesting to the uniformity of the grown film (Figure 3b). X-ray photoemission spectroscopy (XPS) was used to probe the elemental composition and oxidation states of the grown film, as shown in Figure 3c. The spectra exhibit two

DOI: 10.1021/acs.nanolett.8b02688
Nano Lett. 2018, 18, 6340–6346

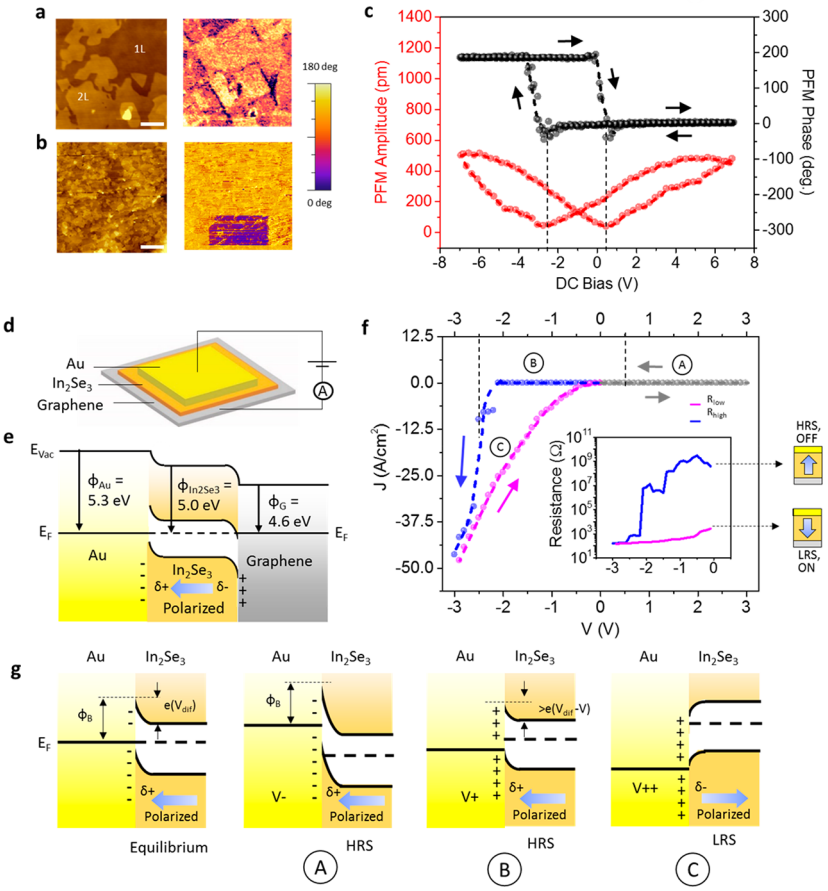

Figure 4. Ferrolectric properties and ferroresistive memory device performance of MBE-grown α-In_2Se_3. (a) Topography and the corresponding PFM-phase image of the as-grown α-In_2Se_3. Scale bar: 1 μm. (b) Topography and the corresponding poled PFM-phase image. An area of 5.2 × 2.5 um^2 is poled by a −6 V biased tip. Scale bar: 2 μm. (c) Local PFM hysteresis curves of the as-grown film. (d) Schematics of the asymmetric ferroelectric memory junction fabricated on the as-grown 6 nm α-In_2Se_3 and its (e) corresponding band diagram alignments at equilibrium. (f) $J(V)$ curve measured from the ferroelectric memory junction with respect to the graphene electrode. The inset shows the corresponding resistance of the blue (0 to −3 V) and pink (−3 to 0 V) curves. (g) Schematics showing the band diagram changes when voltage is applied, in correspondence to the marked A, B, and C regions of the (f) $J(V)$ plot.

doublets with binding energies of 166.5, 160.7, 452.7, and 445.2 eV, which are assigned to the In_2Se_3 XPS peaks for Se $3p_{1/2}$, Se $3p_{3/2}$, In $3d_{3/2}$, and In $3d_{5/2}$ core level orbitals, respectively.[47] The elemental composition of In and Se was obtained by peak fitting with a mixed Gaussian−Lorentzian function after a Shirley background subtraction. XPS chemical composition analysis indicates an In-to-Se ratio of 2:3, confirming the presence of a pure In_2Se_3 phase. There is very little surface oxidation because XPS only detected physisorbed oxygen (Figure S3).

The electronic band gap of the as-grown α-In_2Se_3 sample can be measured using high-resolution electron energy loss spectroscopy (HREELS). The energy-loss region was scanned in a specular geometry with incident electron energy of 16 eV, and the energy gap is determined from the sharp spectral onset delineated by an enhanced intensity from the background, which originates from interband electronic transitions.[48,49] As shown in Figure 3d, an energy onset of ∼1.55 eV was observed, which corresponds to the direct electronic bandgap of α-In_2Se_3.[50] Scanning transmission electron microscopy-annular dark-field (STEM-ADF) image of the monolayer film (Figure 3e) shows a periodic hexagonal *P63/mmc* crystal lattice (Figure S4) with a lattice constant of 4.0 Å, which corresponds to the crystal structure of α-In_2Se_3.[51] Therefore, both spectroscopic and microscopic characterizations unambiguously identified the grown film as the α phase of In_2Se_3.

The piezoelectric and ferroelectric properties of the MBE-grown α-In_2Se_3 were characterized using high-resolution PFM. Figure 4a shows the topography and the corresponding out-of-plane PFM-phase domains of the MBE-grown 1-2L In_2Se_3. The low contrast in the polarization of the PFM phase can be attributed to the small out-of-plane polarization.[5] Notably, the pristine PFM domains are distinct from the topography, indicating that the formation of domains did not arise purely due to topography differences or artifacts in measurement. Spontaneous polarization was induced by a DC bias of −6 V, and a 5.2 μm × 2.5 μm domain was written on the ∼6 nm thick In_2Se_3, which evidence the ferroelectric nature of the film (Figure 4b). Using switching-spectroscopy PFM, a typical ferroelectric butterfly loop and hysteresis loop are observed for the PFM amplitude and PFM phase, respectively (Figure 4c). The measured coercive voltages are approximately +0.5 and −2.5 V.

Giant electroresistance ratio of at least 10^4 is highly desirable for ferroresistive memory device.[2] However, this is rarely observed in nontunneling ferroelectric diode devices.[26] The use of a 2D ferroelectric narrow-band-gap semiconductor allows better tuning of the Schottky barrier through enhancing the

DOI: 10.1021/acs.nanolett.8b02688
Nano Lett. 2018, 18, 6340−6346

Coulomb interactions from its reduced dielectric screening.[52] To further enlarge the differences between the "on"-state and the "off"-state resistance, an asymmetric electrode configuration can be used. To demonstrate such a device, a ferroelectric junction was fabricated on the MBE grown 6 nm film by evaporating gold (Au) electrode on top and using the graphene substrate directly as the bottom electrode, as shown in Figure 4d. The resultant band alignments are shown in Figure 4e. The measured $J(V)$ characteristics with bias applied to the graphene electrode show a rectifying behavior and a strong hysteresis in the negative bias range (Figure 4f), in which a sharp increase of current density is observed at −2.5 V. This value coincides with the switching voltage measured by PFM, which, therefore, indicates that the J(V) behavior is determined by the ferroelectric polarizations. The calculated resistance, R, equals voltage divided by current for the respective forward (blue, 0 V to −3 V) and backward (pink, −3 V to 0 V) measurements and is shown in the inset of Figure 4f. Remarkably, the ratio between the high-resistance state (HRS) and low-resistance state (LRS) is as high as 3.9×10^6, exhibiting a giant electroresistance ratio.[22,53] This device performance demonstrates that few-layer In_2Se_3 ferroelectric semiconductor junction can be used as random access memory, requiring a low voltage of ±4 V to write and approximately −1 V to read. At the reading voltage of −1.4 V, the current density is at least 12 A/cm^2, which is more than 200% higher than typical ferroelectric diode junctions.[1,25] Such high current density can be ascribed to the 2D van der Waals nature of In_2Se_3[54] and provides unambiguous differentiation of the "on" and "off" states for memory sense amplifiers.

It should be noted that α-In_2Se_3 grown on highly ordered pyrolytic graphite (HOPG) substrate gave the same performance as that grown on single layer graphene when fabricated as ferroelectric resistive memory device; thus, the thickness of graphene is not critical to the memory junction performance. The giant electroresistance switching effect can be explained by the interplay of two synergistic factors: (1) the use of 2D van der Waals ferroelectric semiconductor and (2) the use of highly asymmetric electrodes with higher and lower work function than the ferroelectric semiconductor. First, the use of a ferroelectric semiconductor enables the conductivity to be controlled by modulating the width and height of the Schottky barrier[25,55] via the polarization of the ferroelectric. Second, the asymmetric electrodes provide a high rectification ratio. Films thicker than 6 nm were used due to their higher thermal stability and resistance to electron beam-induced damage (Figure 2d). Due to work function differences (UPS of In_2Se_3 in Figure S5), at the metal−semiconductor interfaces, electrons flow from graphene to In_2Se_3 and from In_2Se_3 to Au to form space-charged regions. The asymmetric space-charge interfaces thus result in an intrinsic preferential polarization state in the In_2Se_3 film due to Coulomb interactions (Figure 4e). This also explains the asymmetric coercive voltages measured by PFM. Because In_2Se_3 is an n-type semiconductor (Figure S5), the graphene−In_2Se_3 interface forms an injecting Ohmic contact, and the Au−In_2Se_3 interface forms a Schottky contact, with the potential barrier given as:[56]

$$\phi_B = \phi_M - \chi$$

where ϕ_B is the Schottky barrier, ϕ_M is the work function of metal, and χ is the electron affinity of the semiconductor. ϕ_B is calculated to be 1.7 eV based on the work function of Au as 5.3 eV, and the electron affinity of In_2Se_3 was calculated as 3.6 eV.[57]

Figure 4g illustrates the changes in the Schottky barrier when a voltage bias is applied. At equilibrium, there exists a space-charged depleted region, with a calculated Schottky barrier of ∼1.7 eV. When a negative bias is applied to the Au electrode (positive bias to graphene, as in the Figure 4f plot), the depletion zone width increases.[56] At a voltage bias greater than the coercive voltage (more positive than 0.5 V with respect to graphene), the polarization flips toward the Au electrode and reduces the diffusion potential of the depletion zone. However, the Schottky barrier seen by the transporting electrons does not reduce and electron flow is low (region A of Figure 4f plot). When a positive bias is applied at the Au electrode (the negative region in Figure 4f plot, with respect to graphene), the barrier seen by the electron flow is given by the diffusion potential:[56]

$$e(V_{dif}) = \phi_M - \phi_S$$

where $e(V_{dif})$ is the diffusion potential and ϕ_S is the work function of the semiconductor. It is calculated to be 0.3 eV. With applied bias V, the barrier is reduced by the amount $e(V)$. Because the applied bias still is below that of the coercive voltage for flipping (magnitude lower than −2.5 V), the polarization in In_2Se_3 still points toward the Au electrode and add on to the potential barrier, making it slightly higher than $e(V_{dif} - V)$. As such, it is still in HRS as shown in region B of Figure 4f, and transport is characterized by Schottky emission,[55] with the relationship[56] (Figure S6):

$$I = I_0\left[\exp\left(\frac{eV}{kT}\right) - 1\right]$$

When the magnitude of applied bias is more than the coercive field (−2.5 V with respect to graphene), the polarization in In_2Se_3 reverse and points toward the graphene electrode, resulting in the reversal of the band bending,[22,23] and the transport characteristics is ohmic (Figure S6). The lowest resistance is obtained (region C of Figure 4f) when the ferroelectric polarization direction is parallel to the built-in electric field at the metal−semiconductor interface.[55] It is noted that during discharge, there will be no changes to the injecting ohmic contact at graphene−In_2Se_3; applied bias is distributed across the semiconductor junction, and is not taken up in the contact area, unlike the Schottky contact.[56]

The use of graphene as the substrate serves two purposes. The first is as an epitaxial substrate for the growth of highly crystalline In_2Se_3 films. Another role is to serve as a low-work-function electrode to compliment the high-work-function gold electrode; such an asymmetric electrode design maximizes the polarization effect. In view of the fact that the growth of CVD graphene by roll-to-roll process has entered the first stage of commercialization, the epitaxial growth of ultrathin α-In_2Se_3 on graphene by MBE provides convenient integration in the large-scale fabrication of ferroelectric junctions because high-work-function metal such as gold can be directly sputtered onto α-In_2Se_3−graphene. Another important point is that no "transfer" is needed in this process because the ferroelectric material is directly grown on graphene. Furthermore, the advantage of using α-In_2Se_3 ferroelectric Schottky diode is that no additional engineering of the barrier is needed, unlike the case of FTJ. Highly competitive performances for on−off current and readout diode current can be achieved compared with FTJ and state-of-the-art ferroelectric diodes. The good performance of our ferroelectric junction may be related to the much lower growth temperature used in our MBE growth (250 °C) as compared with CVD methods (>600 °C) because high growth temperature can cause the desorption of highly volatile indium

DOI: 10.1021/acs.nanolett.8b02688
Nano Lett. 2018, 18, 6340−6346

or selenium species, leading to defects and interfacial traps, which affect reproducibility and stability of switchable diode behavior.[58]

In conclusion, we have developed a method to grow large area α-In_2Se_3 films on graphene by MBE, using In_2Se_3 and Se powder precursors and at a low growth temperature of 250 °C. The epitaxial growth grains are highly crystalline and well-oriented, which coalesce to form a uniform and continuous monolayer of α-In_2Se_3. Our MBE growth method can be readily controlled to grow pure phases of monolayer α-In_2Se_3, InSe, and γ-In_2Se_3 as well as mixed phases such as InSe−In_2Se_3. We further designed an asymmetric ferroresistive memory device to exploit the 2D semiconducting ferroelectric nature of α-In_2Se_3 and achieve outstanding performances, with giant electroresistance ratios of 3.9×10^6 and readout current densities of >12 A/cm^2. The successful heteroepitaxial growth of large area ferroelectric semiconductor on graphene at modest growth temperatures allows the convenient fabrication of high-performance ferroelectric Schottky diodes for memory applications.

MBE Growth of Samples. Indium selenides were grown in a customized MBE chamber with a base pressure $\sim 6 \times 10^{-10}$ Torr. Prior to growth, the substrate was degassed in an ultrahigh-vacuum chamber for 30 min and annealed at 600 °C for 5 min. Single-layer graphene on SiO_2/Si is used as the substrate unless otherwise stated. Ultrapure In_2Se_3 powder (99.99%) and Se pellets (99.999%) were evaporated from a crucible heated by an electron beam source and a hot-lip effusion cell, respectively. For the growth of In_2Se_3, the temperature of Se crucible cells was maintained at 150 °C with a hot-lip at 220 °C. The flux ratio of the precursors are as described in the main text. The chamber pressure during growth was $\sim 1 \times 10^{-8}$ Torr when the selenium source is used and $\sim 6 \times 10^{-9}$ Torr when only In_2Se_3 is evaporated.

Atomic Force Microscopy. Atomic force microscopy was performed using Bruker Dimension FastScan Atomic Force Microscope in noncontact mode at room temperature. High-resolution PFM measurements were carried out with a commercial scanning probe microscope (Asylum Research MFP-3D) instrument at ambient atmosphere. Pt-coated tips (AC240TM, spring constant of ~2 N m^{-1}, Olympus, Japan) were used to measure the local switching spectrum and out-of-plane PFM image. The typical scan rate for all scan modes was 1 Hz. The drive frequency, drive amplitude (V_{AC}), and trigger force were ~270 kHz, 1 V, and 80 nN, respectively. To induce polarization in the ferroelectric material, −6 V DC voltage was applied to the conductive tip onto the sample and the sample scanned via normal PFM measurements.

Raman Spectroscopy. Raman spectra were recorded at room temperature using the confocal WiTec Alpha 300R Raman Microscope with laser excitation at 532 nm and power of <100 μW.

Scanning Transmission Electron Microscopy. STEM-ADF imaging was performed using an aberration-corrected JEOL ARM200F, equipped with a cold field emission gun, operating at 80 kV.

High-Resolution Electron Energy-Loss Spectroscopy. HREELS measurements were performed using a Delta 0.5 spectrometer (SPECS, GmbH) with specular geometry in the coarse mode. The impinging electron energy is set to 16 eV with an energy resolution of 30 meV.

X-ray and Ultraviolet Photoemission Spectroscopies. XPS characterizations were performed using SPECS XR-50 X-ray Mg Kα (1253.7 eV) source with a pass energy of 30 eV and a spot size of 5 mm. Detection was done by a PHOIBOS 150 hemispherical energy analyzer (SPECS, GmbH). The binding energies of the XPS spectra were calibrated using Au $4f_{7/2}$ peaks. XPS peak fitting was carried out using a mixed Gaussian−Lorentzian function after a Shirley background subtraction. Area ratios of 3:2 between the In $3d_{5/2}$ and In $3d_{3/2}$ and 2:1 between the Se $3p_{3/2}$ and Se $3p_{1/2}$ peaks were employed in the fit with same full width at half-maximum. UPS measurements were performed with monochromated photon energy of 21.2 eV (He I) and 40.8 eV (He II) through a toroidal mirror monochromator (SPECS GmbH). The detector used is the same as XPS characterizations. The experiments were performed in a chamber of base pressure greater than 5×10^{-10} mbar.

Device Fabrication and Measurements. Top gold electrodes with thicknesses of 50 nm were deposited via thermal evaporation directly on the α-In_2Se_3−graphene samples using a copper grid mask of hole 200 μm × 200 μm. Electrical measurements were carried out at room temperature using Keithley 6430 SourceMeter to record $J(V)$ curves (0 → + 3.0 V → −3.0 V → 0).

■ ASSOCIATED CONTENT

Supporting Information

The Supporting Information is available free of charge on the ACS Publications website at DOI: 10.1021/acs.nanolett.8b02688.

Figures showing MBE growth, desorption of grown α-In_2Se_3, XPS analysis, identification of the structural phase of α-In_2Se_3, UPS of MBE-grown α-In_2Se_3, and conduction mechanisms (PDF)

■ AUTHOR INFORMATION

Corresponding Author

*E-mail: chmlohkp@nus.edu.sg.

ORCID

Sock Mui Poh: 0000-0002-6289-4519
Sherman Jun Rong Tan: 0000-0003-1591-3497
Xiaoxu Zhao: 0000-0001-9746-3770
Jingsheng Chen: 0000-0003-3188-2803
Zhengtang Luo: 0000-0002-4822-9694
Kian Ping Loh: 0000-0002-1491-743X

Author Contributions

○S.M.P. and S.J.R.T. contributed equally. The manuscript was written through contributions of all authors. All authors have given approval to the final version of the manuscript.

Funding

K.P.L. thanks the National Research Foundation, Prime's Minister Office, for support under the midsized Research Centre (CA2DM). We also acknowledge funding support from the Singapore National Research Foundation (NRF) through the Singapore Berkeley Research Initiative for Sustainable Energy (SinBeRISE) Programme.

Notes

The authors declare no competing financial interest.

■ REFERENCES

(1) Jeong, D. S.; Thomas, R.; Katiyar, R. S.; Scott, J. F.; Kohlstedt, H.; Petraru, A.; Hwang, C. S. *Rep. Prog. Phys.* **2012**, *75*, 076502.
(2) Garcia, V.; Bibes, M. *Nat. Commun.* **2014**, *5*, 4289.
(3) Junquera, J.; Ghosez, P. *Nature* **2003**, *422*, 506.

DOI: 10.1021/acs.nanolett.8b02688
Nano Lett. 2018, 18, 6340−6346

(4) Zhou, Y.; Wu, D.; Zhu, Y.; Cho, Y.; He, Q.; Yang, X.; Herrera, K.; Chu, Z.; Han, Y.; Downer, M. C.; Peng, H.; Lai, K. *Nano Lett.* **2017**, *17*, 5508−5513.
(5) Cui, C.; Hu, W.-J.; Yan, X.; Addiego, C.; Gao, W.; Wang, Y.; Wang, Z.; Li, L.; Cheng, Y.; Li, P.; Zhang, X.; Alshareef, H. N.; Wu, T.; Zhu, W.; Pan, X.; Li, L.-J. *Nano Lett.* **2018**, *18*, 1253−1258.
(6) Xue, F.; Zhang, J.; Hu, W.; Hsu, W.-T.; Han, A.; Leung, S.-F.; Huang, J.-K.; Wan, Y.; Liu, S.; Zhang, J.; He, J.-H.; Chang, W.-H.; Wang, Z. L.; Zhang, X.; Li, L.-J. *ACS Nano* **2018**, *12*, 4976−4983.
(7) Xiao, J.; Zhu, H.; Wang, Y.; Feng, W.; Hu, Y.; Dasgupta, A.; Han, Y.; Wang, Y.; Muller, D. A.; Martin, L. W.; Hu, P.; Zhang, X. *Phys. Rev. Lett.* **2018**, *120*, 227601.
(8) Jacobs-Gedrim, R. B.; Shanmugam, M.; Jain, N.; Durcan, C. A.; Murphy, M. T.; Murray, T. M.; Matyi, R. J.; Moore, R. L.; Yu, B. *ACS Nano* **2014**, *8*, 514−521.
(9) Island, J. O.; Blanter, S. I.; Buscema, M.; van der Zant, H. S. J.; Castellanos-Gomez, A. *Nano Lett.* **2015**, *15*, 7853−7858.
(10) Zhai, T.; Fang, X.; Liao, M.; Xu, X.; Li, L.; Liu, B.; Koide, Y.; Ma, Y.; Yao, J.; Bando, Y.; Golberg, D. *ACS Nano* **2010**, *4*, 1596−1602.
(11) Kwon, S. H.; Ahn, B. T.; Kim, S. K.; Yoon, K. H.; Song, J. *Thin Solid Films* **1998**, *323*, 265−269.
(12) Li, H.; Ren, W.; Gao, L.; Wang, G.; Peng, R.; Li, H.; Zhang, P.; Shafa, M.; Tong, X.; Luo, S.; et al. *J. Phys. D: Appl. Phys.* **2016**, *49*, 145108.
(13) Park, S. C.; Lee, D. Y.; Ahn, B. T.; Yoon, K. H.; Song, J. *Sol. Energy Mater. Sol. Cells* **2001**, *69*, 99−105.
(14) Han, G.; Chen, Z. G.; Drennan, J.; Zou, J. *Small* **2014**, *10*, 2747−2765.
(15) Feng, W.; Zheng, W.; Gao, F.; Chen, X.; Liu, G.; Hasan, T.; Cao, W.; Hu, P. *Chem. Mater.* **2016**, *28*, 4278−4283.
(16) Zhou, J.; Zeng, Q.; Lv, D.; Sun, L.; Niu, L.; Fu, W.; Liu, F.; Shen, Z.; Jin, C.; Liu, Z. *Nano Lett.* **2015**, *15*, 6400−6405.
(17) Lin, M.; Wu, D.; Zhou, Y.; Huang, W.; Jiang, W.; Zheng, W.; Zhao, S.; Jin, C.; Guo, Y.; Peng, H.; Liu, Z. *J. Am. Chem. Soc.* **2013**, *135*, 13274−13277.
(18) Okamoto, T.; Yamada, A.; Konagai, M. *J. Cryst. Growth* **1997**, *175−176*, 1045−1050.
(19) Ohtsuka, T.; Okamoto, T.; Yamada, A.; Konagai, M. *Jpn. J. Appl. Phys.* **1999**, *38*, 668.
(20) Ohtsuka, T.; Nakanishi, K.; Okamoto, T.; Yamada, A.; Konagai, M.; Jahn, U. *Jpn. J. Appl. Phys.* **2001**, *40*, 509.
(21) Okamoto, T.; Nakada, Y.; Aoki, T.; Takaba, Y.; Yamada, A.; Konagai, M. *Phys. Status Solidi C* **2006**, *3*, 2796−2799.
(22) Xi, Z.; Ruan, J.; Li, C.; Zheng, C.; Wen, Z.; Dai, J.; Li, A.; Wu, D. *Nat. Commun.* **2017**, *8*, 15217.
(23) Wen, Z.; Li, C.; Wu, D.; Li, A.; Ming, N. *Nat. Mater.* **2013**, *12*, 617.
(24) Yin, Y. W.; Burton, J. D.; Kim, Y. M.; Borisevich, A. Y.; Pennycook, S. J.; Yang, S. M.; Noh, T. W.; Gruverman, A.; Li, X. G.; Tsymbal, E. Y.; Li, Q. *Nat. Mater.* **2013**, *12*, 397.
(25) Jiang, A. Q.; Wang, C.; Jin, K. J.; Liu, X. B.; Scott, J. F.; Hwang, C. S.; Tang, T. A.; Lu, H. B.; Yang, G. Z. *Adv. Mater.* **2011**, *23*, 1277−1281.
(26) Hong, S.; Choi, T.; Jeon, J. H.; Kim, Y.; Lee, H.; Joo, H. Y.; Hwang, I.; Kim, J. S.; Kang, S. O.; Kalinin, S. V.; Park, B. H. *Adv. Mater.* **2013**, *25*, 2339−2343.
(27) Wang, L.; Cho, M. R.; Shin, Y. J.; Kim, J. R.; Das, S.; Yoon, J.-G.; Chung, J.-S.; Noh, T. W. *Nano Lett.* **2016**, *16*, 3911−3918.
(28) Wang, J.-J.; Cao, F.-F.; Jiang, L.; Guo, Y.-G.; Hu, W.-P.; Wan, L.-J. *J. Am. Chem. Soc.* **2009**, *131*, 15602−15603.
(29) Ferrari, A. C. *Solid State Commun.* **2007**, *143*, 47−57.
(30) Li, H.; Zhang, Q.; Yap, C. C. R.; Tay, B. K.; Edwin, T. H. T.; Olivier, A.; Baillargeat, D. *Adv. Funct. Mater.* **2012**, *22*, 1385−1390.
(31) Lei, S.; Ge, L.; Najmaei, S.; George, A.; Kappera, R.; Lou, J.; Chhowalla, M.; Yamaguchi, H.; Gupta, G.; Vajtai, R.; Mohite, A. D.; Ajayan, P. M. *ACS Nano* **2014**, *8*, 1263−1272.
(32) Chen, Y.-l.; Li, M.-l.; Wu, Y.-m.; Li, S.-j.; Lin, Y.; Du, D.-x.; Ding, H.-y.; Pan, N.; Wang, X.-p. *Chin. J. Chem. Phys.* **2017**, *30*, 325−332.
(33) Kambas, K.; Julien, C.; Jouanne, M.; Likforman, A.; Guittard, M. *Phys. Status Solidi B* **1984**, *124*, K105−K108.
(34) Kappera, R.; Voiry, D.; Yalcin, S. E.; Branch, B.; Gupta, G.; Mohite, A. D.; Chhowalla, M. *Nat. Mater.* **2014**, *13*, 1128.
(35) Voiry, D.; Goswami, A.; Kappera, R.; Silva, C. d. C. C. e.; Kaplan, D.; Fujita, T.; Chen, M.; Asefa, T.; Chhowalla, M. *Nat. Chem.* **2015**, *7*, 45.
(36) Tan, S. J. R.; Abdelwahab, I.; Ding, Z.; Zhao, X.; Yang, T.; Loke, G. Z. J.; Lin, H.; Verzhbitskiy, I.; Poh, S. M.; Xu, H.; Nai, C. T.; Zhou, W.; Eda, G.; Jia, B.; Loh, K. P. *J. Am. Chem. Soc.* **2017**, *139*, 2504−2511.
(37) Venables, J. A.; Spiller, G. D. T.; Hanbucken, M. *Rep. Prog. Phys.* **1984**, *47*, 399.
(38) Poh, S. M.; Zhao, X.; Tan, S. J. R.; Fu, D.; Fei, W.; Chu, L.; Jiadong, D.; Zhou, W.; Pennycook, S. J.; Castro Neto, A. H.; Loh, K. P. *ACS Nano* **2018**, *12*, 7562.
(39) Fu, D.; Zhao, X.; Zhang, Y.-Y.; Li, L.; Xu, H.; Jang, A. R.; Yoon, S. I.; Song, P.; Poh, S. M.; Ren, T.; Ding, Z.; Fu, W.; Shin, T. J.; Shin, H. S.; Pantelides, S. T.; Zhou, W.; Loh, K. P. *J. Am. Chem. Soc.* **2017**, *139*, 9392−9400.
(40) Kang, K.; Xie, S.; Huang, L.; Han, Y.; Huang, P. Y.; Mak, K. F.; Kim, C.-J.; Muller, D.; Park, J. *Nature* **2015**, *520*, 656.
(41) Zhou, S.; Tao, X.; Gu, Y. J. *J. Phys. Chem. C* **2016**, *120*, 4753−4758.
(42) Berger, C.; Song, Z.; Li, X.; Wu, X.; Brown, N.; Naud, C.; Mayou, D.; Li, T.; Hass, J.; Marchenkov, A. N.; Conrad, E. H.; First, P. N.; de Heer, W. A. *Science* **2006**, *312*, 1191.
(43) Mahjouri-Samani, M.; Lin, M.-W.; Wang, K.; Lupini, A. R.; Lee, J.; Basile, L.; Boulesbaa, A.; Rouleau, C. M.; Puretzky, A. A.; Ivanov, I. N.; Xiao, K.; Yoon, M.; Geohegan, D. B. *Nat. Commun.* **2015**, *6*, 7749.
(44) Gong, Y.; Ye, G.; Lei, S.; Shi, G.; He, Y.; Lin, J.; Zhang, X.; Vajtai, R.; Pantelides, S. T.; Zhou, W.; Li, B.; Ajayan, P. M. *Adv. Funct. Mater.* **2016**, *26*, 2009−2015.
(45) Poh, S. M.; Tan, S. J. R.; Zhao, X.; Chen, Z.; Abdelwahab, I.; Fu, D.; Xu, H.; Bao, Y.; Zhou, W.; Loh, K. P. *Adv. Mater.* **2017**, *29*, 1605641.
(46) Abidi Irfan, H.; Liu, Y.; Pan, J.; Tyagi, A.; Zhuang, M.; Zhang, Q.; Cagang Aldrine, A.; Weng, L. T.; Sheng, P.; Goddard William, A.; Luo, Z. *Adv. Funct. Mater.* **2017**, *27*, 1700121.
(47) Zheng, Z. Q.; Yao, J. D.; Yang, G. W. *J. Mater. Chem. C* **2016**, *4*, 8094−8103.
(48) Tan Sherman Jun, R.; Abdelwahab, I.; Chu, L.; Poh Sock, M.; Liu, Y.; Lu, J.; Chen, W.; Loh Kian, P. *Adv. Mater.* **2018**, *30*, 1704619.
(49) Vos, M.; King, S. W.; French, B. L. *J. Electron Spectrosc. Relat. Phenom.* **2016**, *212*, 74−80.
(50) Hu, L.; Huang, X. *RSC Adv.* **2017**, *7*, 55034−55043.
(51) In2Se3 crystal structure, phases. In *Ternary Compounds, Organic Semiconductors*; Madelung, O.; Rössler, U.; Schulz, M., Eds.; Springer Berlin Heidelberg: Berlin, Germany, 2000; pp 1−5.
(52) Mak, K. F.; He, K.; Lee, C.; Lee, G. H.; Hone, J.; Heinz, T. F.; Shan, J. *Nat. Mater.* **2013**, *12*, 207.
(53) Zhuravlev, M. Y.; Sabirianov, R. F.; Jaswal, S. S.; Tsymbal, E. Y. *Phys. Rev. Lett.* **2005**, *94*, 246802.
(54) Lembke, D.; Kis, A. *ACS Nano* **2012**, *6*, 10070−10075.
(55) Blom, P. W. M.; Wolf, R. M.; Cillessen, J. F. M.; Krijn, M. P. C. M. *Phys. Rev. Lett.* **1994**, *73*, 2107−2110.
(56) Van der Ziel, A. *Solid State Physical Electronics*, 3rd ed.; Prentice-Hall Inc: Englewood Cliffs, NJ, 1976.
(57) Drapak, S. I.; Kovalyuk, Z. D.; Netyaga, V. V.; Orletskii, V. B. *Tech. Phys. Lett.* **2002**, *28*, 707−710.
(58) Fan, Z.; Fan, H.; Lu, Z.; Li, P.; Huang, Z.; Tian, G.; Yang, L.; Yao, J.; Chen, C.; Chen, D.; Yan, Z.; Lu, X.; Gao, X.; Liu, J.-M. *Phys. Rev. Appl.* **2017**, *7*, 014020.

DOI: 10.1021/acs.nanolett.8b02688
Nano Lett. 2018, 18, 6340−6346